1

Positron emission tomography image reconstruction using feature extraction

Juan Gao[a,1], Qiyang Zhang[a,b,1], Qiegen Liu[c], Xuezhu Zhang[d], Mengxi Zhang[d], Yongfeng Yang[a], Dong Liang[a], Xin Liu[a], Hairong Zheng[a] and Zhanli Hu[a,*]

[a]*Lauterbur Research Center for Biomedical Imaging, Shenzhen Institute of Advanced Technology, Chinese Academy of Sciences, Shenzhen, China*
[b]*Shenzhen College of Advanced Technology, University of Chinese Academy of Sciences, Shenzhen, China*
[c]*Department of Electronic Information Engineering, Nanchang University, Nanchang, China*
[d]*Department of Biomedical Engineering, University of California, Davis, CA, USA*

Abstract.

PURPOSE: To reduce the cost of positron emission tomography (PET) scanning systems, image reconstruction algorithms for low-sampled data have been extensively studied. However, the current method based on total variation (TV) minimization regularization nested in the maximum likelihood-expectation maximization (MLEM) algorithm cannot distinguish true structures from noise resulting losing some fine features in the images. Thus, this work aims to recover fine features lost in the MLEM-TV algorithm from low-sampled data.

METHOD: A feature refinement (FR) approach previously developed for statistical interior computed tomography (CT) reconstruction is applied to PET imaging to recover fine features in this study. The proposed method starts with a constant initial image and the FR step is performed after each MLEM-TV iteration to extract the desired structural information lost during TV minimization. A feature descriptor is specifically designed to distinguish structure from noise and artifacts. A modified steepest descent method is adopted to minimize the objective function. After evaluating the impacts of different patch sizes on the outcome of the presented method, an optimal patch size of 7×7 is selected in this study to balance structure-detection ability and computational efficiency.

RESULTS: Applying MLEM-TV-FR algorithm to the simulated brain PET imaging using an emission activity phantom, a standard Shepp-Logan phantom, and mouse results in the increased peak signal-to-noise ratio (PSNR) and structural similarity (SSIM) as comparing to using the conventional MLEM-TV algorithm, as well as the substantial reduction of the used sampling numbers, which improves the computational efficiency.

CONCLUSIONS: The presented algorithm can achieve image quality superior to that of the MLEM and MLEM-TV approaches in terms of the preservation of fine structure and the suppression of undesired artifacts and noise, indicating its useful potential for low-sampled data in PET imaging.

Keywords: Positron emission tomography (PET), maximum likelihood-expectation maximization (MLEM), low-sampled data, total variation (TV), feature extraction

---

[1]These authors contributed equally to this work.

*Corresponding author: Zhanli Hu, Lauterbur Research Center for Biomedical Imaging, Shenzhen Institute of Advanced Technology, Chinese Academy of Sciences, Shenzhen 518055, China. E-mail: zl.hu@siat.ac.cn.

1. Introduction

In clinical practice, positron emission tomography (PET) imaging has become more widely used and has achieved promising effects. PET scanners are relatively expensive imaging systems for patients and clinicians in regional and community centers [1]. One of the ways to reduce the scanner cost is to reduce the number of detectors [2]. However, PET image reconstruction obtains an accurate estimation of the radiotracer distribution in an object from the detected photons; therefore, image reconstruction to obtain high-diagnostic PET images from low-sampled data is a challenging task [3].

Assuming that sampling data have a Poisson distribution, iterative statistical reconstruction methods are able to model the physical detection process [2]. In addition, iterative reconstruction can make use of noise statistics, accurate system modeling, and image prior knowledge via comparison to analytical reconstructions [4]. Therefore, to improve image quality, iterative reconstruction methods have been increasingly used in PET imaging [3–9]. However, from the perspective of statistical inference, the maximum likelihood-expectation maximization (MLEM) algorithm [8, 9], which estimates images from projections by seeking the maximum likelihood (ML) solution, results in increased noise once the iteration reaches a certain point, especially for low-sampled data. To reduce the increased noise, methods that filter the images from a higher number of iterations and various constraints that regularize the radiotracer distribution have been implemented [10–12]. Nevertheless, such approaches cannot yield reconstructed images with sharp edges but blur the reconstruction [12].

To overcome this challenge, an alternative approach in signal processing is the use of compressive sensing (CS) techniques [13–17]. Because the image/signal can be represented by sparse coefficients in an alternative domain [18], CS enables the recovery of images/signals from fewer measurements than those governed by the traditional Nyquist sampling theorem. Most CS methods use predefined sparsifying transform domains, such as wavelets, curvelets, and finite transforms. However, the gradient magnitude domain is one of the very commonly used sparsifying transform domains [19–22], in which a piecewise constant assumption (PCA) is used as the underlying assumption. Therefore, total variation (TV) minimization regularization with sparse gradients based on CS theory was derived as a denoising technology and nested in the MLEM method to suppress noise while maintaining sharp edges (MLEM-TV) [6, 12, 23, 24]. However, the TV constraint is a global requirement that cannot adequately represent the structures of an object. Moreover, PCA often generates patchy artifacts, and the gradient operator cannot distinguish true structures from image noise. For this reason, TV-based reconstruction algorithms may lose some fine structures and generate a blocky appearance, particularly for low-sampled data. To overcome these problems, Muller et al. improved the MLEM-TV algorithm using an inverse scale space method that uses Bregman distances [7, 25]; the method can restore the loss of contrast in the images. Wang and Qi proposed a patch-based regularization method that can preserve features or textures within patches [4]. Yang et al. designed a shift-variant quadratic penalty function in penalized maximum-likelihood (PML) image reconstruction to improve lesion detectability [6]. Tang et al. proposed a dictionary learning (DL)-based sparse signal representation in the formation of the prior for MAP PET image reconstruction that achieved improved bias and contrast at comparable levels of noise [12].

Recently, we developed a statistical interior tomography approach for computed tomography (CT) reconstruction [26], in which an interior feature refinement (FR) step is performed after each iteration of penalized weighed least-square TV (PWLS-TV) to recover the desired features lost during TV minimization. The potential usefulness of the approach has been verified for noise suppression and feature preservation of interior tomography with truncated projection measurements. Motivated by this study, an FR was embedded in the MLEM-TV approach preliminarily verified in the reference [27], which is performed after each MLEM-TV iteration for low-sampled data to remove the patchy artifacts and preserve fine features. For simplicity, the presented method is called "MLEM-TV-FR".

The proposed method aims to make PCA unnecessary and to restore the fine structure via statistical modeling and iterative FR.

The remaining sections of the paper are organized as follows. Section 2 describes the MLEM-TV reconstruction, feature refinement and evaluation method, in which the feature refinement step is introduced in detail; the pseudocode for the presented MLEM-TV-FR method is also outlined in this section. In Section 3, the experimental setup, the emission activity brain phantom study, the 2D Shepp-Logan phantom and mouse data, quantitative evaluation, parameter evaluation, and the results are reported, followed by the Discussion and Conclusion sections.

2. Method

2.1. MLEM-TV Reconstruction

The measured emission sinogram data y is a vector in which each element y_i contains the number of counts accumulated in bin i during a PET scan. The measurement y can be assumed to be a collection of independent Poisson random variables because of the countable nature of the annihilation events[12], which can be modeled by a Poisson distribution with mean $\bar{y}_i$:

$$P(y_i | \bar{y}_i) = \frac{e^{-\bar{y}_i} \bar{y}_i^{y_i}}{y_i!} \tag{1}$$

in which $\bar{y}_i$, the mean of the measurement data, is related to the unknown activity distribution map x by an affine transform:

$$\bar{y} \approx Gx + r \tag{2}$$

where $G = \{g_{i,j}\} \in \mathcal{R}^{I \times J}$ is the system matrix, in which I and J are the number of PET measurements and image pixels, respectively, and r is the model of the random and scatter coincidences. Thus, the ML estimate of the activity distribution map x is the solution that maximizes the log of the likelihood function, which is written as follows [3, 8]:

$$L(x | y) = \sum_{i=1}^{I} \left(y_i ln \left(\sum_{j=1}^{J} g_{i,j} x_j \right) - \sum_{j=1}^{J} g_{i,j} x_j \right) \text{such that } x \geq 0 \tag{3}$$

$L(x | y)$ can be maximized using the iterative MLEM algorithm. MLEM starts with the full-ones image as an initial estimation of x and gradually converges to the solution using the following update function:

$$x^{n+1} = \frac{x^n}{S} G^T \frac{y}{Gx^n + r} \tag{4}$$

in which n is the iteration number and $S = \left(\sum_{i=1}^{I} g_{i,j} \right)^T$ is the sensitivity image.

To suppress the increased noise in the MLEM iteration, TV minimization regularizations are widely used. The TV of the image, taking advantage of the image gradient magnitude sparseness, is one of the most commonly used methods:

$$TV(x) = \sum_{s,t} \sqrt{(x_{s,t} - x_{s-1,t})^2 + (x_{s,t} - x_{s,t-1})^2 + \alpha} \tag{5}$$

Here, s and t are the indices of the location of the desired tracer distribution map, and a is a small constant used to maintain differentiability with respect to image intensity ($\alpha = 1 \times 10^{-8}$ in our work).

In this paper, the TV-regularized MLEM algorithm, which can be solved using the steepest descent method, is referred to as "MLEM-TV".

97   *2.2. Feature refinement (FR)*

In clinical practice, small-scale and low-contrast structures are very important for diagnosis. However, some fine structures in reconstruction using the MLEM-TV method are likely to be lost for the gradient operator, especially for low-sampled data. To extract the fine features from missing structures, we propose an FR step that is conducted after each MLEM-TV iteration, as described in the following equation:

$$x_{FR} = x + f_t \otimes \upsilon \tag{6}$$

where $x_F R$ is the feature-refined image, x is the TV-minimized image before FR, and υ is the residual image between two successive iterations of TV minimization. The symbol $\otimes$ denotes pointwise multiplication. f_t denotes a feature descriptor, which is defined as:

$$f_t = 1 - \left| \frac{2\sigma_{qp} + C}{\sigma_p^2 + \sigma_q^2 + C} \right| \tag{7}$$

98   in which the constant C is introduced for numerical stability ($C = 1.25 \times 10^{-6}$ in our work). The local

99   statistics σ_p, σ_q and σ_{pq} at pixel R are defined as $\sigma_p(j) = \left(\frac{1}{N-1} \sum_{j \in p_j} (x(j) - P(j))^2 \right)^{1/2}$, $\sigma_q(j) =$

100    $\left(\frac{1}{N-1} \sum_{j \in q_j} (x_d(j) - Q(j))^2 \right)^{1/2}$ and $\sigma_{qp}(j) = \frac{1}{N-1} \sum_{j \in (p_j, q_j)} (x(j) - P(j))(x_d(j) - Q(j))$, in

101   which $P(j) = \frac{1}{N} \sum_{j \in p_j} x(j)$, $Q(j) = \frac{1}{N} \sum_{j \in q_j} x_d(j)$, where p_j and q_j denote two local image

102   patches of size $\sqrt{N} \times \sqrt{N}$ centered at pixel j; these images are extracted from x, and a degraded

103   image x_d is obtained by a linear Gaussian filter from x. Here, the parameters of the Gaussian filter

104   function are as follows: the standard deviation is 10, and the rotation angle is 0. The nature of the

105   proposed model structure descriptor involves a contrast variation component and a structure corre-

106   lation component. The former calculates the reduction of contrast variation caused by the degrading

107   operation, and the latter quantifies the structural correction between the original and degraded images.

108   The value of each element in the feature descriptor image f_t is in the interval [0, 1], and a larger value

109   is correlated with a higher likelihood of belonging to part of the structure. The proposed approach is

110   referred to as "MLEM-TV-FR" and consists of the following three main steps:

111   1) *Initial estimate:* The full-ones image is used as the initial estimate x^0.

112   2) *MLEM-TV cost function minimization:* Given the current tracer distribution image estimation

113   x^n, the steepest descent method is used to yield a new image estimation, i.e., x_{tv}^n, which can be

114   expressed as follows:

$$x_{tv}^n = x^n - \beta \times \nabla TV(x^n) \tag{8}$$

115   where $\nabla TV(x^n)$ represents the gradient of $TV(x^n)$, and β represents the gradient step size ($\beta = 0.01$ in

116   our work).

117   3) *Feature refinement:* After each iteration of MLEM-TV, the reconstruction result x_{tv}^n is replaced

118   by x_{FR}^n, as obtained by the feature refinement step $x_{FR}^n = x_{tv}^n + f_t^n \otimes v^n$, where x_{FR}^n is the feature-

119   refined image, and $v^n = x^n - x_{tv}^n$ is the residual image between two successive iterations of TV

120   minimization. f_t^n is the feature descriptor extracted from x_{tv}^n, and $f_t^n \otimes v^n$ is the detected structure

121   image. Finally, $x^{n+1} = x_{FR}^n$ is updated.

122   In the implementation, x^{n+1} was outputted until the stopping criterion was satisfied, which was

123   solved by a modified gradient descent algorithm [28]. Moreover, to find a stable convergent solution,

Table 1
Pseudocode for the MLEM-TV-FR method

1: **Initialization**:
 $x_{FR}^0 = ones$;
2: **While** a stopping criterion is not met;
3: $x^{n-1} = x_{FR}^{n-1}$;
4: update image estimation x^n using (4);
5: obtain a new image estimation x_{tv}^n using (8);
6: repeat step 5;
7: calculate the residual image:
 $v^n = x^n - x_{tv}^n$;
8: calculate the feature descriptor f_t^n from x_{tv}^n using (7);
9: extract the structure information from the residual image and refine the image estimation:
 $x_{FR}^n = x_{tv}^n + f_t^n \otimes v^n$
10: repeat steps 6–9, $n = n + 1$;
11: **End**.

the peak signal-to-noise ratio (PSNR) metric and the structural similarity index (SSIM) were used to measure the reconstructed image quality. In summary, the pseudocode for the presented MLEM-TV-FR method can be described in Table 1.

Since the feature descriptor, which is designed to distinguish structures from noise and artifacts, plays an important role in our proposed algorithm, several scalar parameters should be carefully tuned in our MLEM-TV-FR algorithm. For example, an image patch size of 7×7 is a good choice for balancing structure-detection capacity and computational efficiency. Additionally, the parameter C is included to avoid instability when $\sigma_p^2 + \sigma_q^2$ is very close to zero. Therefore, it should be assigned a small constant ($C = 1.25 \times 10^{-6}$ in our work).

2.3. Evaluation

1) *Evaluation by noise reduction*. Peak signal to noise ratio (PSNR) was adopted to evaluate the noise reduction capabilities of different reconstruction algorithms, and it is given as follows:

$$PSNR = 10 \, log_{10} \left[\frac{MAX^2 (x_{true})}{\sum_{m=1}^{Q} (x(m) - x_{true}(m))^2 / (Q - 1)} \right] \tag{9}$$

where x represents the reconstructed image, x_{true} represents the true image, m indexes the pixels of the image, $MAX(x_{true})$ denotes the maximum intensity value of x_{true}, and Q is the total number of pixels in the image.

2) *Evaluation by quantitative image quality degradation*. Structural similarity (SSIM), which is a perceptual metric that quantifies image quality degradation, was used to measure the perceptual difference between the reference image and the reconstructed image, and it is given as follows:

$$SSIM(x, y) = \frac{(2\mu_x\mu_y + C_1)(2\sigma_x\sigma_y + C_2)}{\left(\mu_x^2 + \mu_y^2 + C_1\right)\left(\sigma_x^2 + \sigma_y^2 + C_2\right)} \tag{10}$$

where x and y represent the reconstructed image and the reference image or true image, respectively, μ_x and μ_y represent the average gray value of the image, and σ_x and σ_y represent the standard deviation

Table 2
Sampling number

Object of study	Idea sampling number of MLEM	Used sampling number of MLEM-TV-FR
Brain phantom	258 radial bins × 384 sample angles	172 radial bins × 64 sample angles
Shepp-Logan	258 radial bins × 384 sample angles	172 radial bins × 128 sample angles
Mouse	62208 counts	7776 counts

of the image. The constants C_1 and C_2 are introduced for numerical stability ($C_1 = 2.55^2$ and $C_2 = 7.65^2$ in our work).

3. Experiments and results

An emission activity brain phantom, 2D Shepp-Logan phantom and mouse data study were designed to evaluate the performance of MLEM-TV-FR and to compare it with those of MLEM-TV and conventional MLEM algorithms. During the implementation of existing algorithms and the proposed MLEM-TV-FR algorithm, the full-ones image is used as the initial value of the first iteration. For simulated and mouse data, Table 2 shows the idea sampling number needed for the MLEM method and the sampling number used for the proposed method. In addition, SSIM and PSNR are used to evaluate the reconstruction parameter and the performance of the proposed method.

All algorithms used in the present work were implemented in the MATLAB R2014a programming environment. The code is run on a 64-bit Ubuntu 15.10 operating system with an Intel® Xeon (R) CPU E5-2643 v3 @ 3.40 GHz × 24 and 32 GB of memory.

3.1. Brain phantom experiment setup

In this experiment, an emission activity brain phantom image is used for the simulation study (shown in Fig. 1) to compare the performance of the proposed algorithm with those of the MLEM-TV and conventional MLEM algorithms. The image matrix size is 256×256, and the pixel size is 1.9531×1.9531 mm. The emission activity brain phantom image (shown in Fig. 1) was forward-projected with dimensions of 258 (radial bins) × 384 (sample angles) and 172 (radial bins) × 64 (sample angles) to obtain the sinogram data. To further verify the performance of the algorithm, Gaussian noise (the mean and variance are 0.01 and 0.0001, respectively) was added to the image domain of the brain phantom in this experiment as a new set of comparative experiments.

3.2. Brain phantom experiment results

In the simulation, the superior performance of the presented MLEM-TV-FR algorithm is verified by comparing the images reconstructed by the MLEM, MLEM-TV, and MLEM-TV-FR methods (shown in Fig. 2). In Fig. 2, the first row shows the full-sampled reconstruction result, the second row is the low-sampled reconstruction result, and the third row is the low-sampled reconstruction result of the brain image with Gaussian noise; the first column is the reconstruction result of the MLEM algorithm, the second column is the reconstruction result of the MLEM-TV algorithm, and the third column is the reconstruction result of MLEM-TV-FR. The MLEM-reconstructed image (a-labeled images in Fig. 2) contains serious artifacts and distinct noise. Moreover, although the result of MLEM-TV (b-labeled images in Fig. 2) exhibits fewer artifacts and less noise, it diminishes the fine structure.
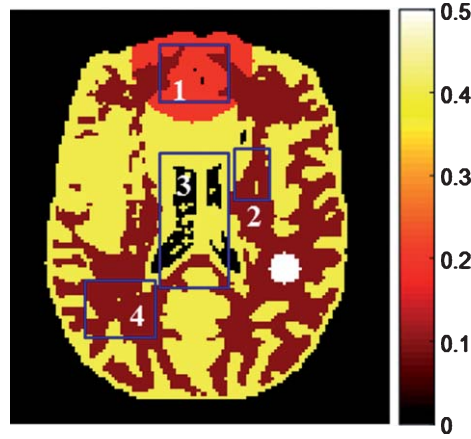
Fig. 1. Emission activity brain phantom image.

175 However, the reconstruction using the MLEM-TV-FR method (c-labeled images in Fig. 2) shows
176 considerable benefits relative to MLEM-TV in terms of preserving small-scale and low-contrast struc-
177 tures. Figure 3 shows the zoomed 2.5 ROIs (regions of interest) of the reconstruction results shown in
178 Fig. 2. Here, ROIs are the areas inside the four blue boxes in Fig. 1. In Fig. 3, ROI_1–ROI_4 are the ROIs of
179 the real image, and a_{11}–a_{14}, b_{11}–a_{14}, and c_{11}–c_{14} are the ROIs of the full-sampled image reconstructed
180 by the MLEM algorithm, the MLEM-TV algorithm, and the MLEM-TV-FR algorithm, respectively.
181 In addition, a_{21}–a_{24}, b_{21}–b_{24}, and c_{21}–c_{24} are the ROIs of the low-sampled image reconstructed by the
182 MLEM, MLEM-TV and MLEM-TV-FR algorithms, respectively. In addition, a_{31}–a_{34}, b_{31}–b_{34}, and
183 c_{31}–c_{34} are the ROIs of low-sampled images with Gaussian noise reconstructed by the MLEM-TV,
184 MLEM-TV and MLEM-TV-FR algorithms, respectively. The MLEM algorithm adds severe noise
185 and artifacts in full-sample reconstruction from a_{11}–a_{14}, and the low-sampled reconstructions from the
186 MLEM algorithm not only add serious noise and artifacts but also lose some of the fine structure shown
187 in the zoomed ROIs a_{21}–a_{24} and a_{31}–a_{34}. The zoomed ROIs b_{11}–a_{14}, b_{21}–b_{24}, and b_{31}–b_{34} show that
188 the MLEM-TV algorithm can suppress noise and artifacts but loses fine features; the MLEM-TV-FR
189 algorithm can retain some fine features while suppressing noise and artifacts. In the low-sampled recon-
190 struction with Gaussian noise, the MLEM-TV-FR algorithm still shows relatively good reconstruction
191 capability, as shown in c_{31}–c_{34}.

192 *3.3. Brain phantom experiment quantitative evaluation*

193 The PSNR and SSIM values are computed across 2000 iterations to compare the performances of the
194 MLEM, MLEM-TV and MLEM-TV-FR algorithms. Figure 4 shows the evaluation results of noise-free
195 low-sampled reconstruction, and Fig. 5 shows the evaluation results of low-sampled reconstruction
196 with Gaussian noise. Here, the black dashed boxes are partial enlarged views. While updating the
197 reconstructed image, although the MLEM-TV-FR method converges more slowly, its PSNR and SSIM
198 values are the largest, i.e., its noise reduction effect is optimal, and its result is the best-quality image
199 in this work.

200 *3.4. Shepp-Logan phantom experiment setup*

201 To validate the performance of this study, the presented method was applied to simulated data using
202 a 2D Shepp-Logan phantom (shown in Fig. 6). The image matrix size is 256×256, and the pixel
203 size is 1.9531×1.9531 mm. First, the reference image of the Shepp-Logan phantom was obtained by
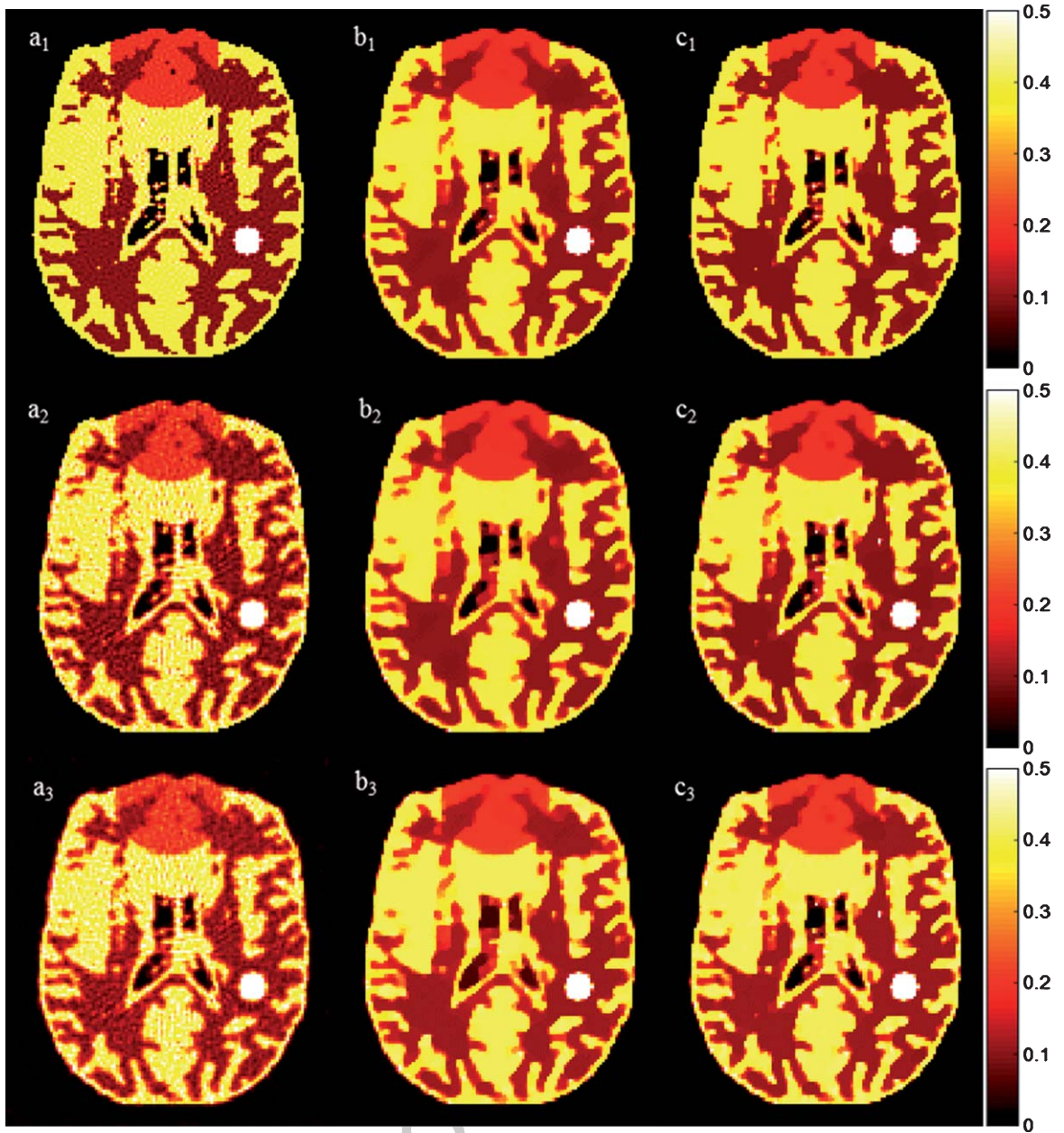
Fig. 2. Brain reconstruction images. The first row shows the full-sampled reconstruction result, the second row is the low-sampled reconstruction result, and the third row is the low-sampled reconstruction result of the brain image with Gaussian noise. The first column is the reconstruction result of the MLEM algorithm, the second column is the reconstruction result of the MLEM-TV algorithm, and the third column is the reconstruction result of the MLEM-TV-FR algorithm.

the MLEM method from 258 (radial bins) × 384 (sample angles) sinogram data acquired by forward-projection for the 2D Shepp-Logan phantom without noise, which is shown in Fig. 7(a). Then, the 172 (radial bins) × 128 (sample angles) sinogram data were acquired by forward-projection with the Shepp-Logan phantom and added to independent Poisson noise.
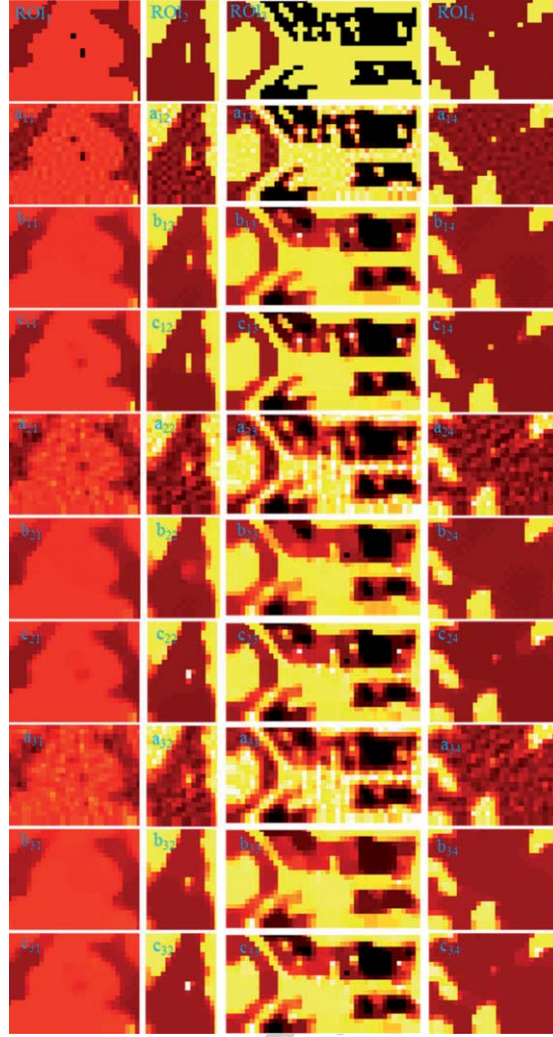
Fig. 3. Zoomed (2.5 times) ROIs. The ROIs are the areas inside the four blue boxes shown in Fig. 1. ROI_1–ROI_4 are the zoomed ROIs of the real image. All a-labeled images are zoomed ROIs of the MLEM-reconstructed results. All b-labeled images are zoomed ROIs of the MLEM-TV-reconstructed results. All c-labeled images are zoomed ROIs of the MLEM-TV-FR-reconstructed results. In addition, a_{11}–a_{14}, b_{11}–b_{14}, and c_{11}–c_{14} are the ROIs of the full-sampled images, a_{21}–a_{24}, b_{21}–b_{24}, and c_{21}–c_{24} are the ROIs of the low-sampled images, and a_{31}–a_{34}, b_{31}–b_{34}, and c_{31}–c_{34} are the ROIs of the low-sampled reconstruction images with Gaussian noise. All images are displayed with the same window.

3.5. Shepp-Logan phantom experiment results

Figure 7 shows 2D Shepp-Logan reconstruction images by the MLEM, MLEM-TV and MLEM-TV-FR methods from the 172 (radial bins) $\times$ 128 (sample angles) sinogram data with noise. Figure 7(a) is the reference image. The artifacts and noise in Fig. 7(b) acquired by the MLEM method are severe. Figure 7(c), reconstructed by the MLEM-TV method, is blurry because some of the fine structure is lost during the reconstruction process. Figure 7(d), obtained by the MLEM-TV-FR method, reduces noise, suppresses artifacts and retains fine structures. The tops of each image in Fig. 7 are detailed views indicated in the red dashed box. The MLEM-TV-FR method retains the details that are lost using the MLEM-TV method, as indicated by the red arrows in the top of Fig. 7(d).
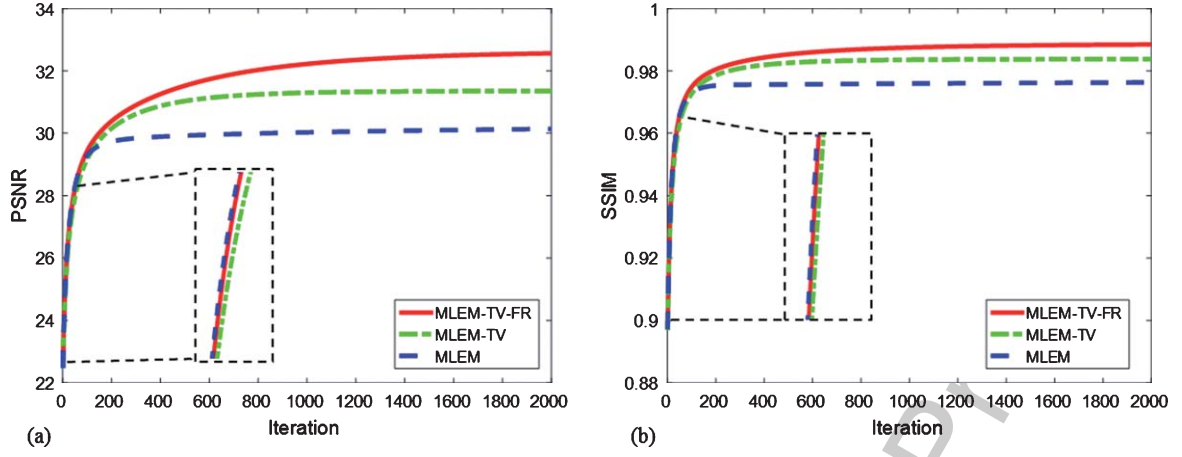
Fig. 4. Evaluation of noise-free low-sampled reconstruction. (a) PSNR (b) SSIM.
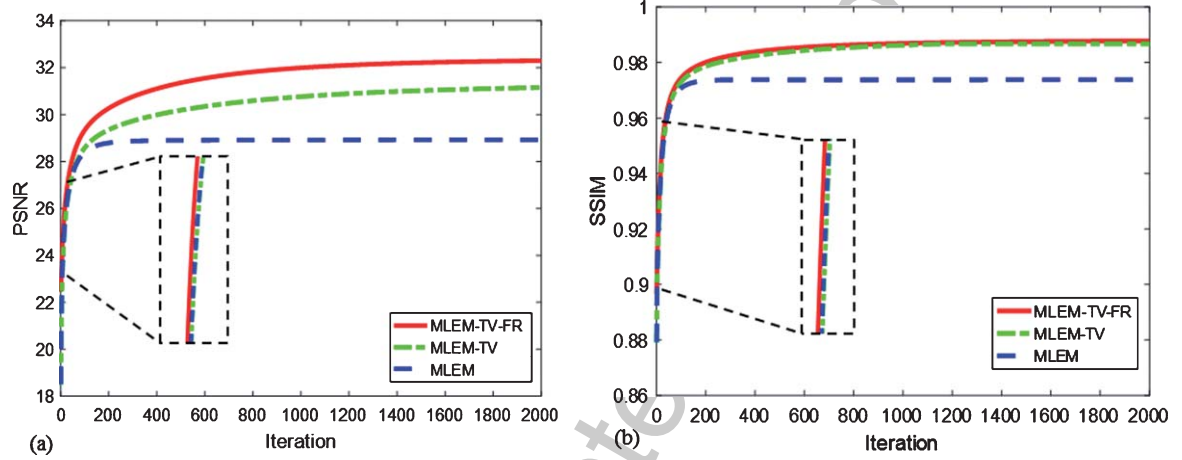

Fig. 5. Evaluation of low-sampled reconstruction with Gaussian noise. (a) PSNR (b) SSIM.
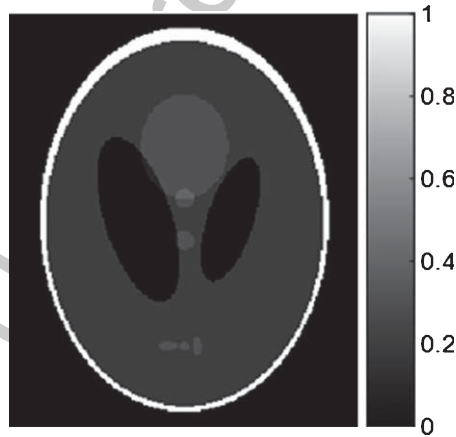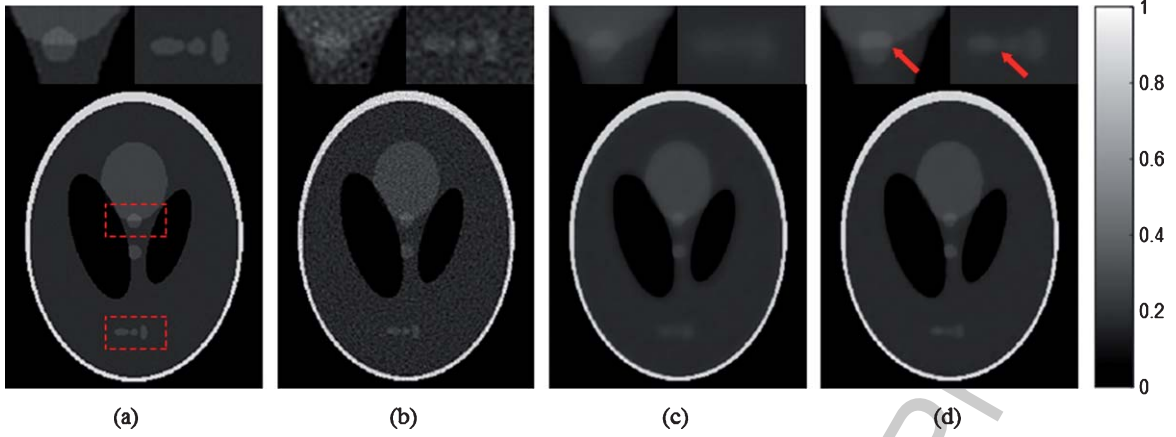

Fig. 6. Shepp-Logan phantom image.

Fig. 7. Shepp-Logan images reconstructed from the low-sampled noisy data using different methods and 1000 iterations. The tops of the images are detailed views indicated in the red dashed box. (a) Reference (MLEM reconstruction image from the normal-count data without noise), (b) MLEM, (c) MLEM-TV, and (d) MLEM-TV-FR.

3.6. Mouse data study

In this work, 21 MBq of ^{18}F-fluorodeoxyglucose was injected into a 19.4 g mouse. Thirty min after injection, the mouse was scanned on the Inveon D-PET scanner for 15 min. No scatter or attenuation correction was performed in this study.

Two sets of contrast experiments, one set with full-sample reconstructed images and the other set with low-sampled reconstructed images (one-eighth of the full-sample data is used as low-sampled data), were designed. The proposed algorithm was evaluated with the MLEM and MLEM-TV methods by comparing their reconstructed images from full-sample data and low-sampled data. Figure 8 shows the reconstructed results by different reconstruction methods, where the first row is the full-sample reconstruction image, and the second row is the low-sampled reconstruction image. The first column is the reconstruction result of the MLEM algorithm, the second column is the reconstruction result of the MLEM-TV algorithm, and the third column is the reconstruction result of the MLEM-TV-FR algorithm. Figure 9 shows a zoomed (2 times) ROI for each image in Fig. 8; here, the ROI is the area inside the white dashed box in Fig. 8. The MLEM images are noisy and affected by the low-sampling data, while MLEM-TV achieves better performance regarding noise reduction but results in the degradation of the small-scale and low-contrast structures of the image. However, the presented MLEM-TV-FR method can suppress noise and achieve high low-contrast detestability, as shown in the zoomed ROIs.

3.7. Parameter evaluation

In addition to visualization-based evaluation, we analyzed the sensitivity of the MLEM-TV-FR algorithm to parameter settings by varying patch size, as parameter C has little effect on the performance of the proposed algorithm. Fixing parameter C at 1.25×10^{-6}, reconstructions were performed when the patch size increased from 3 to 47.

Figure 10 shows the impact of patch size on MLEM-TV-FR. The PSNR and SSIM values do not change linearly as patch size increases. PSNR is higher when the patch size is between 5×5 and 9×9, and when the patch size is larger than 27×27, PSNR is almost constant. From the local point of view, SSIM is higher between 11×11 and 15×15, and when the patch size is larger than 27×27, the SSIM grows slowly to an almost horizontal state. To balance structure-detection ability and computational
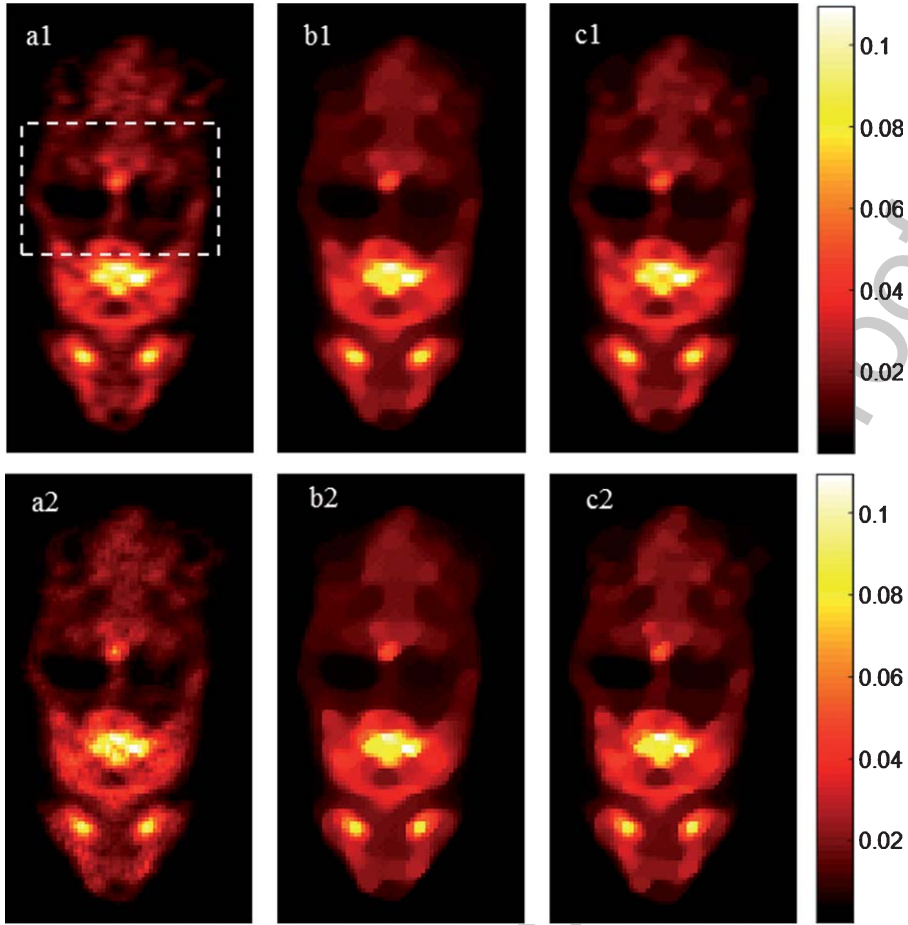
Fig. 8. Reconstructed results from mouse data. Image a1, b1, and c1 are the reconstruction results of the MLEM, MLEM-TV, and MLEM-TV-FR algorithms from the full-sample data, respectively. Images a2, b2, and c2 are the reconstruction results of the MLEM, MLEM-TV, and MLEM-TV-FR algorithms from the low-sampled data, respectively.
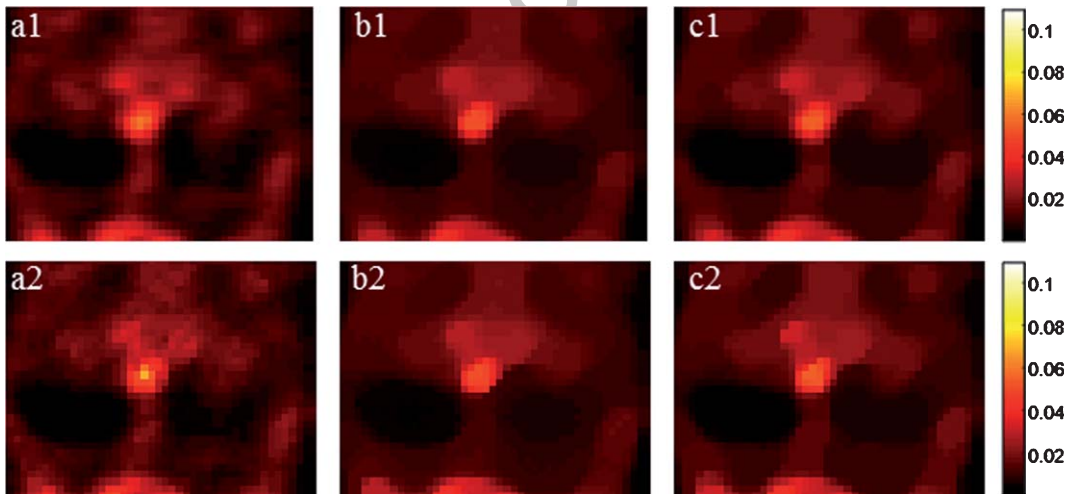

Fig. 9. Zoomed (2 times) ROIs of the mouse reconstruction results are shown in Fig. 8. The ROI is the area inside the white dashed box in Fig. 8.
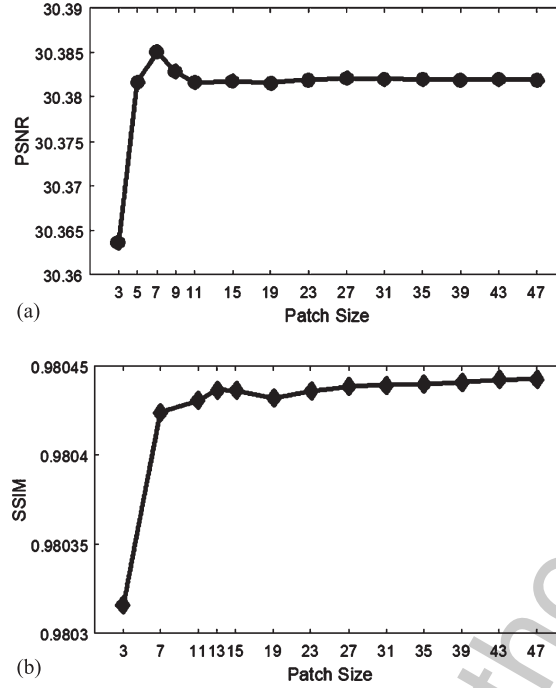
Fig. 10. Parameter evaluation. (a) PSNR versus patch size. (b) SSIM versus patch size.

efficiency, a patch size between 7×7 and 15×15 is suggested. The image patch size in our experiments was 7×7.

4. Discussion

We developed a fine-structure recovery model for PET images from low-sampled data based on the TV minimization model. The model was validated by computer simulations and the study of mouse data. In addition, we evaluated the impacts of different patch sizes on the outcome of the presented method. The MLEM-TV-FR algorithm is robust with regard to patch size and can achieve an image quality superior to that of the MLEM and MLEM-TV approaches in terms of the preservation of the fine structure and the suppression of undesired artifacts and noise, which indicates its useful potential for low-sampled data in PET imaging.

In practice, several complex factors, such as data calibration and noise, will unavoidably violate the data piecewise constant assumption [26]. In this poor condition, the MLEM-TV algorithm produces blocky results and may lose some fine features for noisy and low-sampled data owing to the piecewise constant image model. In contrast, the FR step aims to simultaneously recover the fine structures lost in TV minimization, suppress noise and reduce artifacts.

In general, the number of iterations required for the algorithm to converge depends on the complexity of the algorithm and that of the image and noise. The OSEM method is a fast statistical iterative algorithm that divides the projection data into a finite subset and solves its ML estimate on each subset to accelerate convergence. The OSEM-based method overcomes the slow convergence of the MLEM-based algorithm. To avoid artifacts, the subset balance should be guaranteed. However, in the actual measurement process, it is difficult to achieve subset balance, which will affect the quality of the reconstructed image. To better analyze the performance of the FR step in each iteration, this work adopts MLEM-TV instead of OSEM-TV. Because each iteration in the presented MLEM-TV-FR

method contains one MLEM calculation, three TV minimization calculations and two FR extraction calculations, the complexity of the proposed algorithm is greater than that of the MLEM-TV method. Considering the time efficiency, we set a maximum number of iterations (in this work, it is 2000) as a stopping criterion to constrain convergence. The PSNR and SSIM results in Figs. 4 and 5 show that the proposed algorithm has almost converged at 2000 iterations, indicating that our stopping criterion is reasonable. The convergence of the MLEM-TV-FR method is slow because the signal-to-noise ratio (SNR) of the PET image is low, and it is very difficult to extract fine features using the FR step. Moreover, the MLEM algorithm for low-sampled data results in increased noise once the iteration reaches a certain point and produces a wrong estimation. Therefore, three TV minimization calculations were performed after one MLEM calculation during the implementation of the presented algorithm, and the FR step was used to extract useful features from the residual image between two successive iterations in TV minimization.

One limitation of this work is that the proposed MLEM-TV-FR method adds computational burdens because of the feature refinement step. A GPU accelerator can be used to accelerate the computation of the presented algorithm. In future work, we will further improve the FR method so that it can be applied to advanced PET reconstruction algorithms to study clinical experiments.

Acknowledgments

References

[1] S.M. W, T. I, Makrilia, M. N and S. K, Role and cost effectiveness of PET/CT in management of patients with cancer, *Physics in Medicine and Biology* **83** (2010), 53–65.

[2] S. Valiollahzadeh, J.W. Clark and O. Mawlawi, Dictionary learning for data recovery in positron emission tomography, *Physics in Medicine and Biology* **60** (2015), 5853–5871.

[3] G.B. Wang and J.Y. Qi, PET image reconstruction using kernel method, *IEEE Transactions on Medical Imaging* **34** (2015), 61–71.

[4] G. Wang and J. Qi, Penalized likelihood PET image reconstruction using patch-based edge-preserving regularization, *IEEE Transactions on Medical Imaging* **31** (2012), 2194–2204.

[5] J. Qi and R.M. Leahy, Iterative reconstruction techniques in emission computed tomography, *Physics in Medicine and Biology* **51** (2006), R541.

[6] L. Yang, A. Ferrero, R.J. Hagge, R.D. Badawi and J. Qi, "Evaluation of penalty design in penalized maximum-likelihood image reconstruction for lesion detection, *Journal of Medical Imaging* **1** (2014), 035501.

[7] J. Muller, C. Brune, A. Sawatzky, T. Kosters, K.P. Schafers and M. Burger, Reconstruction of Short Time PET Scans Using Bregman Iterations, *2011 IEEE Nuclear Science Symposium and Medical Imaging Conference*, 2011, pp. 2383–2385.

[8] L.A. Shepp and Y. Vardi, Maximum likelihood reconstruction for emission tomography, *IEEE Transactions on Medical Imaging* **1** (1982), 113–122.

[9] K. Lange and R. Carson, EM reconstruction algorithms for emission and transmission tomography, *Journal of Computer Assisted Tomography* **8** (1984), 306–316.

[10] J.A. Fessler, Penalized weighted least-squares image reconstruction for positron emission tomography, *IEEE Transactions on Medical Imaging* **13** (1994), 290–300.

[11] S. Ahn and R.M. Leahy, Analysis of resolution and noise properties of nonquadratically regularized image reconstruction methods for PET, *IEEE Transactions on Medical Imaging* **27** (2008), 413–424.

[12] J. Tang, B. Yang, Y. Wang and L. Ying, Sparsity-constrained PET image reconstruction with learned dictionaries, *Physics in Medicine and Biology* **61** (2016), 6347–6368.

[13] S. Ahn, S.M. Kim, J. Son, D.S. Lee and J.S. Lee, Gap compensation during PET image reconstruction by constrained, total variation minimization, *Medical Physics* **39** (2012), 589–602.

[14] S. Valiollahzadeh, J.W. Clark and O. Mawlawi, Using compressive sensing to recover images from PET scanners with partial detector rings, *Medical Physics* **42** (2015), 121–133.

[15] S. Valiollahzadeh, J. Clark and O. Mawlawi, Dictionary learning in compressed sensing using undersampled data in PET imaging, *Medical Physics* **40** (2013), 400.

[16] D. Richter, T.C. Basse-Lusebrink, T. Kampf, A. Fischer, I. Israel, M. Schneider, P.M. Jakob and S. Samnick, Compressed sensing for reduction of noise and artefacts in direct PET image reconstruction, *Medical Physics* **24** (2014), 16–26.

[17] P. Olcott, E. Kim, G. Chinn and C. Levin, Compressed sensing for the multiplexing of large area silicon photomultiplier PET detectors: Acquisition and calibration, *Journal of Nuclear Medicine* **53** (2012), 2388.

[18] D.L. Donoho, Compressed sensing, *IEEE Trans Inf Theory* **52** (2006), 1289–1306.

[19] E.Y. Sidky and X. Pan, Image reconstruction in circular cone-beam computed tomography by constrained, total-variation minimization, *Physics in Medicine and Biology* **53** (2008), 4777.

[20] X. Pan, E.Y. Sidky and M. Vannier, Why do commercial CT scanners still employ traditional, filtered back-projection for image reconstruction? *Inverse Problems* **25** (2009), 123009.

[21] S. Ahn, S.M. Kim, J. Son, D.S. Lee and J. Sung Lee, Gap compensation during PET image reconstruction by constrained, total variation minimization, *Medical Physics* **39** (2012), 589–602.

[22] Y. Wang and Z. Qi, A new adaptive-weighted total variation sparse-view computed tomography image reconstruction with local improved gradient information, *Journal of X-ray Science and Technology* **26** (2018), 957–975.

[23] A. Sawatzky, C. Brune, F. Wubbeling, T. Kosters, K. Schafers and M. Burger, Accurate EM-TV Algorithm in PET with Low SNR, *2008 IEEE Nuclear Science Symposium and Medical Imaging Conference (2008 Nss/Mic)*, Vols 1-9, 2009, p. 4399.

[24] M. Burger, K. Frick, S. Osher and O. Scherzer, Inverse total variation flow, *Multiscale Model Sim* **6** (2007), 366–395.

[25] C. Brune, A. Sawatzky and M. Burger, Primal and dual bregman methods with application to optical nanoscopy, *Int J Comput Vision* **92** (2011), 211–229.

[26] Z. Hu, Y. Zhang, J. Liu, J. Ma, H. Zheng and D. Liang, A feature refinement approach for statistical interior CT reconstruction, *Physics in Medicine and Biology* **61** (2016), 5311–5334.

[27] Z.L. Hu, J. Gao, D. Liang, X. Liu, H.R. Zheng and Y.F. Yang, PET Image Reconstruction from Under-sampled Data, *2017 IEEE Nuclear Science Symposium and Medical Imaging Conference*, 2017.

[28] J.A. O'Sullivan and J. Benac, Alternating minimization algorithms for transmission tomography, *IEEE Transactions on Medical Imaging* **26** (2007), 283–297.